# Role of electrostatic doping on the resistance of metal and two-dimensional materials edge contacts

Madhuchhanda Brahma,[1] Maarten L. Van de Put,[1] Edward Chen,[2] Massimo V. Fischetti,[1] and William G. Vandenberghe[1]

[1]*Department of Materials Science and Engineering, The University of Texas at Dallas, 800 W. Campbell Road, Richardson, Texas 75080, USA*

[2]*Corporate Research, Taiwan Semiconductor Manufacturing Company Ltd., 168, Park Avenue II, Hsinchu Science Park, Hsinchu 300-75, Taiwan*

(Received 25 January 2024; accepted 29 July 2024; published 10 September 2024)

In this theoretical study, we compare electrostatically doped metal-transition metal dichalcogenide (TMD) edge-contacts versus substitutionally doped edge-contacts in terms of their contact resistance. Our approach involves the utilization of electrostatic doping achieved by applying back-gate bias to the metal-TMD edge contacts, where carrier injection is primarily governed by the Schottky barrier at the interface. To analyze these contacts, we employ the Wentzel-Kramers-Brillouin (WKB) approximation to calculate the transmission coefficient and use density functional theory (DFT)-derived band structures. We numerically solve the Poisson equation to capture the electrostatic potential. We also account for the impact of the image force using Green's function for the Poisson equation with boundary conditions appropriate to our specific geometry. Our findings reveal that electrostatically doped TMD edge contacts exhibit higher contact resistance compared to impurity-doped edge contacts at equivalent carrier concentrations. At the same time, we find that, among the electrostatically doped edge contacts, a low-$\kappa$ back-gate oxide in conjunction with low-$\kappa$ top oxide is preferable in terms of improvement in contact resistance. For instance, in a metal-TMD edge contact scenario involving a monolayer $MoS_2$ as the channel, $SiO_2$ as the infinitely thick top oxide, and a $SiO_2$ back-gate oxide with an equivalent oxide thickness (EOT) of 1 nm, we demonstrate that it is possible to achieve an impressively low contact resistance of 50 Ω μm when the back-gate bias exceeds or equals 2 V.

DOI: 10.1103/PhysRevResearch.6.033278

## I. INTRODUCTION

Two-dimensional (2D) materials, particularly transition-metal dichalcogenides (TMDs), has ignited excitement for the future of electronic devices [1,2–11]. These materials offer unique electronic properties due to their flat structure making them prime candidates for efficient current flow in devices. However, the realization of TMD-based devices faces many difficulties, among which is the problem of obtaining a low resistance for the Schottky metal-TMD contacts that usually exhibit a high barrier [7,12–16].

Theoretical studies employing quantum-transport models based on density functional theory (DFT) have shed light on how metals and semiconductors interact at an atomic scale, impacting Schottky barrier height and carrier injection [17–20]. However, these simulations face computational challenges, especially when dealing with wide depletion regions and therefore limit applicability. Additionally, an essential phenomenon in metal-semiconductor contacts, known as image-force barrier lowering (IFBL), remains beyond DFT's scope. This effect, which plays a role in all metal-semiconductor contacts, cannot be overlooked in calculating contact resistance.

Previously [21], we have shown how the surrounding dielectric material strongly affects the contact resistance in 2D materials by modulating the depletion length as well as the Schottky barrier lowering due to image charges. We found that image-force barrier lowering in 2D material contacts doesn't follow the traditional bulk formula. Unlike in bulk materials, in 2D edge-contact devices, the dielectric properties of both the surrounding oxide and the TMD itself dictate the image-force barrier lowering. Additionally, we demonstrated that the bond strength between different metals and 2D materials has a weaker impact on contact resistance compared to the surrounding dielectric material. Our key finding emphasized the importance of using low-$\kappa$ surrounding dielectrics, combined with a high doping and low Schottky barrier, to improve contact resistance in 2D materials, though there remains a question as to how to address scaling which typically requires a high-$\kappa$ dielectric material. In our study [21] we found that metal-to-n-type $MoS_2$ edge-contacts with $SiO_2$ as top and bottom insulators, a doping concentration $>1\times10^{13}$ cm$^{-2}$ and a metal work-function $<5.1$ eV yielded impressively low contact resistance down to 50 Ω μm. Conversely, we found that high-$\kappa$ dielectrics such as $HfO_2$ worsened the contact resistance due to longer depletion width and reduced image-force barrier lowering.

Degenerately doping 2D materials is a promising strategy for minimizing contact resistance. Traditional ion-implantation methods, while effective, have been observed to compromise the integrity of monolayer transition metal dichalcogenides (TMDs), resulting in defect formation. This has spurred the exploration of innovative doping methods for 2D TMDs. The main techniques involve substitutional doping, charge transfer doping, and electrostatic doping. The achievement of high levels of doping in TMDs has commonly involved n or p type substitutional doping, accomplished through controlled source or environmental conditions during *in situ* TMD fabrication [22–26] or, alternatively, using chemical vapor deposition (CVD) techniques [27–30]. Nonetheless, substitutional doping has been identified as a source of surface and lattice defects, adversely affecting TMD device performance [31].

The limitations associated with substitutional doping are circumvented by charge-transfer doping. In this method, dopants, such as gaseous molecules, metals, or organic molecules, adsorb onto the TMDs. The resulting doping type, whether n-type or p-type, depends on the direction of charge transfer dictated by the difference of Fermi levels between the TMDs and the dopants [32–34].

Last, electrostatic doping, a nondestructive, reversible doping approach, presents a promising option. In this technique, modulation of the charge within the TMDs is achieved through gate voltage manipulation. By manipulating the charge within TMDs through gate voltage adjustments, this approach exploits the capacitive coupling between an external gate and TMDs [35–37]. Electrostatic doping in TMDs is typically achieved through back-gating. However the intricate interplay between back-gating and image-force barrier-lowering, and their implications for contact resistance, requires further exploration.

In this paper, we assess quantitatively the contact resistance in 2D material edge-contacts within the context of back-gated electrostatic doping. We take into account the effect of the back gate and the nonuniform dielectric environment on the Poisson equation. Additionally, we consider the reduction of the IFBL effect due to the screening caused by the back gate. We find that low-$\kappa$ bottom-gate oxide in conjunction with a low-$\kappa$ top dielectric reduces the contact resistance. However, back-gating is not as effective as conventional doping in reducing the contact resistance. Therefore, electrostatic doping may not provide the definitive solution for enhancing metal-TMD contacts.

## II. METHOD

We perform our simulations on the edge-contact geometry shown in Fig. 1(a), composed of a semi-infinite undoped TMD monolayer "sandwiched" between an infinitely thick top oxide ($SiO_2$ or $HfO_2$) and a thin bottom-oxide with a metal back-gate. Following our previous work [21], we assume an ideal Schottky barrier excluding effects due to interface chemistry of the contacts, Fermi-level pinning, or band-offsets, which allows us to treat the junction in a simplified way and at the same time incorporate the effect of the back-gate oxides and barrier lowering due to surrounding dielectric. We choose very thick (50 nm) dielectric as the top insulator to reduce any effects from Neumann boundary conditions on the electrostatics of the monolayer TMD [21]. The thickness of the TMD monolayer ($MoS_2$ in this study) has been extracted from the relaxed structure in the DFT calculation. In Fig. 1(b) we show the various edge contact geometries that we have simulated in this work. For simplicity and convenience for the readers, we refer to the different device configurations as: A, B, C, D, E, and F. It should be noted that A, B, C, and D have back-gate (i.e., electrostatically doped), whereas E, F denote the geometries used in our previous work (i.e., without back-gate, doped channel). Based on the conclusion of our previous work, i.e., low-$\kappa$ dielectric environment favors lower contact resistance, we choose to use $SiO_2$ as the infinitely thick top oxide in our current work (except C). However, for the sake of comparison with our previous work where we used the same high-$\kappa$ dielectric as the top and bottom oxides, we also calculate the contact resistances using $HfO_2$ as the top and bottom oxides, denoted as geometry C. For the back-gate oxide, we choose either $SiO_2$ or $HfO_2$. It should be noted that since a back-gate oxide as $SiO_2$ with EOT of 1 nm is subjected to considerable gate leakage, we also simulate a device with a similar configuration as A but with an effective oxide thickness (EOT) of 4 nm (schematic of structure not shown).

In our previous work [21] we compared contact resistances calculated using the WKB approximation to that obtained by the NEGF formalism. We established that the WKB results match closely with the NEGF results using "ideal" contacts [21], with a slight overestimation in the conductance. Moreover, as mentioned in our previous work, a treatment of 2D contacts that takes into account the dielectrics requires a large simulation domain (as the depletion width is of the order of 200 nm), which renders full scale DFT-NEGF simulations hugely prohibitive. Additionally, it is not possible to treat image-force barrier lowering using DFT-NEGF simulations. Therefore, here we use the WKB approximation to obtain the transmission probability through the Schottky barrier at the metal-TMD junction. We obtain the contact resistance by the following equation [38]:

$$\frac{1}{\rho_c} = \int_{-\infty}^{\infty} \frac{2e^2}{h} \left\{ \int \left[ \sum_n M_n(k_y, E) T_n(k_y, E) \right] \frac{dk_y}{2\pi} \right\} \times \left| \frac{\partial f(E)}{\partial E} \right| dE, \tag{1}$$

where $\rho_c$ denotes the contact resistance, $e$ is the electronic charge, $h$ is the Planck's constant, $n$ is the band index for the monolayer TMD, $k_y$ is the parallel wave-vector, and $f(E)$ is the Fermi-Dirac distribution function. $E(k_y)$ has been calculated from the full band DFT energy band-dispersion using Wannier interpolation [39]. $T(k_y, E)$ is the transmission probability as a function of energy $E$ and $k_y$. $M(k_y, E)$ denotes the number of conducting channels at the energy of interest, and would result in the ballistic conductance in the absence of the WKB integral.

The calculation of the WKB tunneling probability requires the knowledge of the electrostatic potential. We calculate this 2D depletion potential by solving the Poisson equation with Dirichlet boundary conditions at the metal contact and back gate, using FEniCS [40,41]. We assume an anisotropic

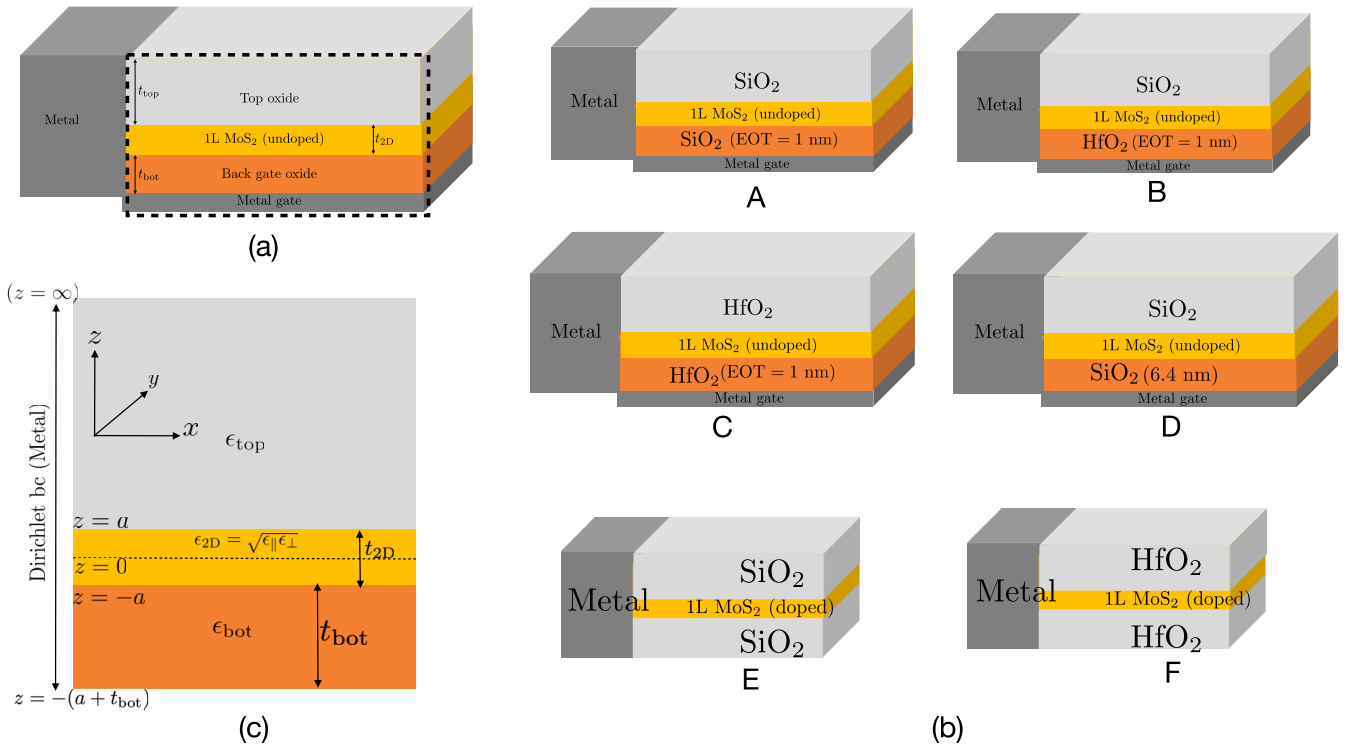


FIG. 1. (a) Edge-contact geometry considered in current work, where the middle layer is undoped monolayer $MoS_2$ with a thickness $t_{2D}$ sandwiched between infinitely thick ($t_{top} \gg t_{bot}, t_{top} \gg t_{2D}$) top insulator and a bottom insulator of finite thickness $t_{bot}$. The Poisson equation is solved over the 2D cross-section marked as a dashed box. (b) The different edge-contact geometries considered in the simulation are described here. A, B, and C denote the back-gated edge-contacts where the EOT of the back-gate oxides are 1 nm. D has a similar composition as A, but the back-gate oxide has a thickness equal to the physical thickness of $HfO_2$ with EOT 1 nm. A, B, and D comprise of infinitely thick top insulator $SiO_2$ with back-gate oxides as $SiO_2$ or $HfO_2$, whereas C has $HfO_2$ as both the infinitely thick top insulator and back-gate oxide. E and F represent the geometries without back gate considered in our previous work [21], where E and F stand for $MoS_2$ monolayers "sandwiched" between infinitely thick $SiO_2$ and $HfO_2$ respectively. (c) Schematic of the structure where we compute the Coulomb kernel with a point charge located at $z = 0$. The top and bottom oxides have a homogenous isotropic permittivity, whereas the middle (2D) semiconductor has an anisotropic permittivity.

dielectric permittivity for $MoS_2$ [42] The charge density inside the channel is computed numerically by solving the 2D Poisson equation self-consistently with the TMD-full band density-of-states obtained from DFT.

We calculate the band structure of monolayer $MoS_2$, using the DFT package Vienna *ab initio* Simulation Package (VASP) [43–46]. We first use the generalized gradient approximation (GGA) with the projector-augmented wave (PAW) method [47] using the Perdew-Burke-Ernzerhof (PBE) exchange-correlation functional [48] for geometry optimization until the maximum force on every atom drops below 0.01 eV/Å. We keep a large vacuum space of 30 Å along the $z$ direction to avoid interaction between successive layers. We also include the DFT-D3 dispersion correction of Grimme [49] to describe van der Waals interactions and calculate accurately the interlayer distance. Next, we use the relaxed structure to run electronic calculations using Heyd-Scuseria-Ernzerhof (HSE06) hybrid functional [50] with spin-orbit coupling and an electronic convergence of $10^{-6}$ eV, sampled on the Brillouin zone with a Γ-centered 8×8×1 $k$-mesh. We interpolate the band structure on a denser 20×20×1 $k$-mesh by using Maximally localized Wannier Functions in the Wannier90 code [39] and use it to compute the transmission probability.

We calculate the image charge potential in the geometry shown in Fig. 1(c), analytically by solving the Coulomb kernel of a point charge inside $MoS_2$ using the Hankel transform [21]:

$$\hat{V}_{\text{image}}(Q, z=0) = -\frac{[\epsilon_{2D}\cosh(aQ) + \epsilon_{top}\sinh(aQ)][\epsilon_{2D}\cosh(aQ)\sinh(t_{bot}Q) + \epsilon_{bot}\sinh(aQ)\cosh(t_{bot}Q)]}{\epsilon_{2D}Q\left[\epsilon_{top}\epsilon_{bot}\cosh(t_{bot}Q) + {\epsilon_{2D}}^2\sinh(t_{bot}Q) + \epsilon_{2D}\cosh(2aQ)\{\epsilon_{bot}\cosh(t_{bot}Q) + \epsilon_{top}\sinh(t_{bot}Q)\}\right]} \quad (2)$$

and the method of images to obtain the image potential energy. In Eq. (2), $\epsilon_{2D}$, $\epsilon_{top}$, and $\epsilon_{bot}$ represent the dielectric permittivities of the 2D material, top and bottom oxides, respectively, whereas $a$, $t_{top}$, and $t_{bot}$ denote one-half of the 2D material thickness, the top and bottom oxide thicknesses, respectively.

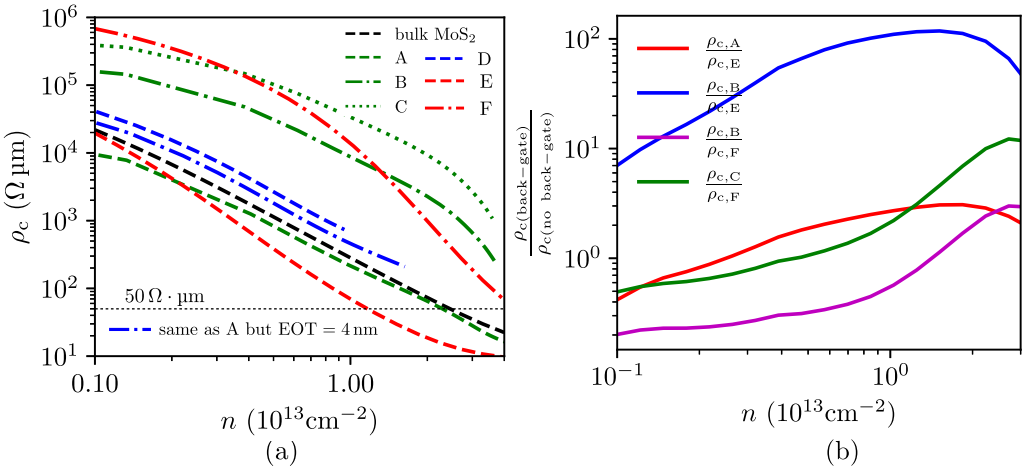


FIG. 2. (a) Calculated contact resistance vs doping concentration for $MoS_2$ edge-contacts with a Schottky barrier height of 0.3 eV. The top $x$ axis denotes the bulk doping concentration in $MoS_2$. The lowest contact resistance is achieved with top and bottom insulators as $SiO_2$ in configurations with both back gate and without back gate. i.e., A and E. The blue lines do not span the entire density range because we limit back-gate bias to 4 V. (b) Ratio of contact resistances of configurations A, B, and C as a function of doping concentration, to their nongate counterparts E and F.

## III. RESULTS

Figure 2(a) shows the plot between contact resistance and doping concentration. We compare both bulk contact (without gate) and edge-contact configurations, with and without back gate. Additionally, we analyze the ratio of contact resistances with and without the back gate in Fig. 2(b), all at a Schottky barrier height of 0.3 eV. We obtain the contact resistance for the devices (E and F) excluding the effect of electrostatic doping (simulated with infinitely thick top and bottom oxide) from our previous work [21]. The most favorable contact resistance is achieved in impurity-doped edge-contacts surrounded by a low-$\kappa$ dielectric (outperforming bulk contacts), denoted as geometry E. Among the back-gated devices, device A, with $SiO_2$ as the top and bottom oxides shows the lowest contact resistance. It slightly surpasses the performance of bulk configurations, and overall demonstrates the smallest reduction in contact resistance with respect to its nongated counterpart E. As $SiO_2$ back-gate oxide with EOT of 1 nm can lead to higher gate leakage in practical cases, we simulated a similar configuration with EOT of 4 nm which is shown as blue dash-dotted line in Fig. 2(a). It has a contact resistance which is slightly higher than A, but lower than other back-gate configurations. A doping concentration of $2\times10^{13}$ cm$^{-2}$ is sufficient to achieve a contact resistance as low as 50 Ω μm in edge-contact configuration A, whereas much higher doping concentrations are required to attain the same contact resistance in the other electrostatically doped configurations.

Figure 2(b) shows that the contact resistance in A increases upto a factor of 2.5 with respect to its no-gate counterpart E. A similar trend is observed for configuration C, which utilizes the same high-$\kappa$ top and bottom insulators, as its no-gate counterpart F. Notably, the contact resistance in this setup is 11 times higher, clearly illustrating the adverse impact of back-gating. These patterns of increased contact resistance in back-gated edge-contacts persist across configurations. In geometry B, the back-gate oxide material is the same high-$\kappa$ dielectric as used in F and a low-$\kappa$ top oxide similar to E. We have shown the ratio of its contact resistance with respect to both E and F. An analysis of geometry B reveals a 2.5-fold rise in contact resistance in relation to geometry F, and a substantial 100-times increase with respect to geometry E. Thus, it becomes clear that electrostatically doped edge-contacts demonstrate a higher contact resistance than substitutionally doped edge-contacts. Among the electrostatically doped contacts, at a given EOT, where the top oxide material remains same (i.e., A and B), we find that A, which has a low-$\kappa$ back-gate oxide, performs better. On comparing B and C, i.e., configurations with same EOT and same high-$\kappa$ dielectric back-gate oxide but different top dielectric, we find that C, which has $HfO_2$ as the top oxide, exhibits a worse contact resistance. The analysis of the contact resistance configurations shown in Fig. 2 thereby underscores the crucial roles played by doping concentration, dielectric environment and back-gating in guiding the optimization of contacts in 2D materials.

The choice of back-gate oxide proves to be a pivotal factor influencing contact resistance through the depletion width and image-force barrier-lowering (IFBL). In Fig. 4, we observe the influence of distinct dielectric environments on the depletion width. Specifically, at a given EOT, the largest depletion width is observed when both the back-gate oxide and the thick top oxides are high-$\kappa$ dielectrics. This phenomenon is further demonstrated in the contour plots displayed in Figs. 3(a), 3(b), and 3(c) that show the 2D potential within electrostatically doped configurations A, B, and C with electric field lines superimposed. The potential spreads slowly over the length of the channel as the surrounding dielectric permittivity increases and the charge transfer across the metal-semiconductor junction occurs over a longer distance. This leads to a larger tail of the depletion width inside the 2D channel. Figures 3(d), 3(e), and 3(f) show that the electric field is strongest in geometry A where both the top dielectric and the back-gate oxide is $SiO_2$. The presence of a high-$\kappa$ material as the top- or back-gate oxide increases the electric field screening as shown in Fig. 3(e) and 3(f). Further, a

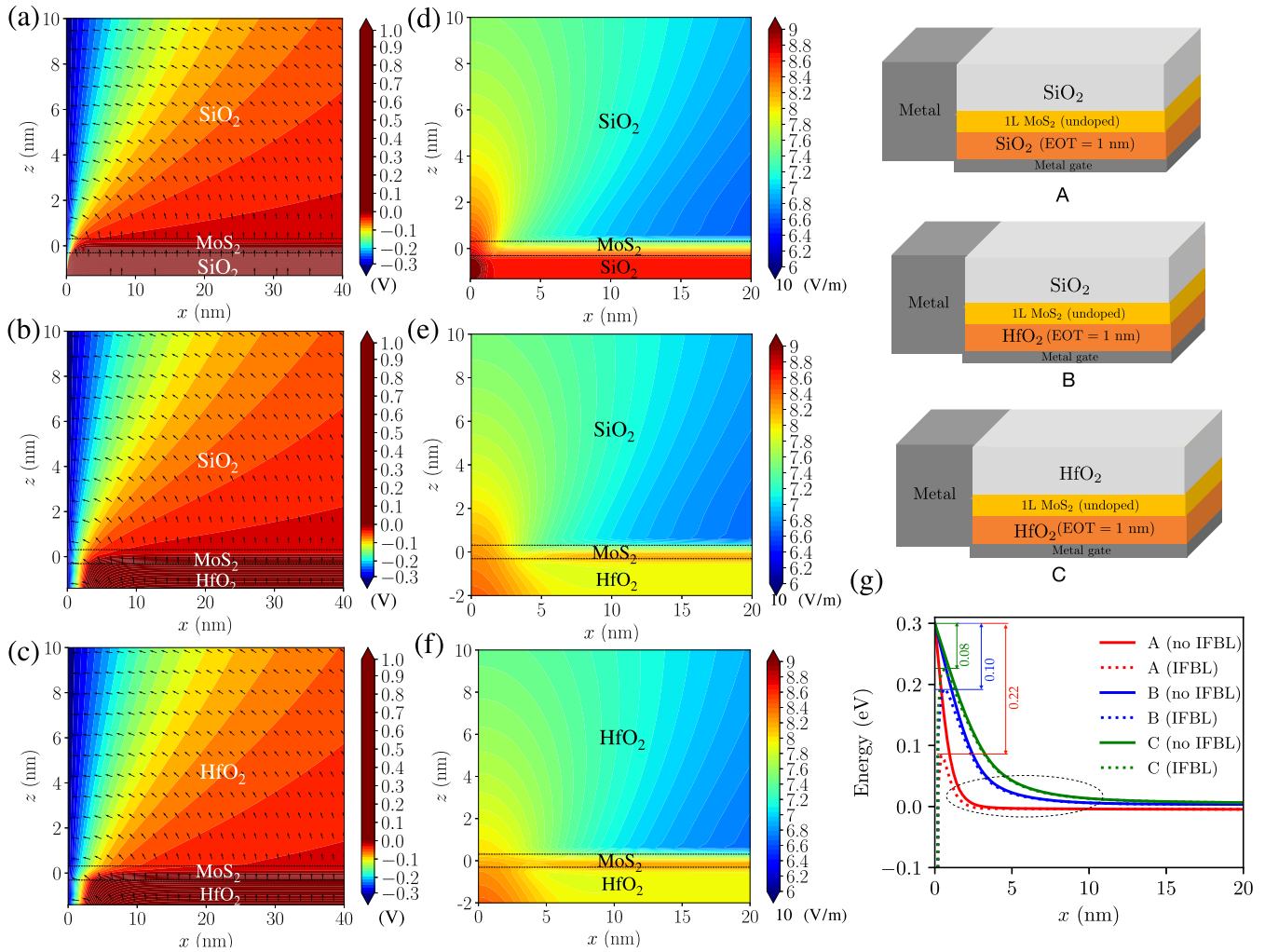


FIG. 3. Contour plots of potential with electric field lines in a 2D cross-section of electrostatically doped (back-gate) edge-contact geometries (a) A, (b) B, and (c) C, and, magnitude of electric field in a cross-section of electrostatically doped (back-gate) edge-contact geometries (d) A, (e) B, and (f) C, at a Schottky barrier height of 0.3 eV and $V_{BG} = 1$ V. The region between the dotted black lines is the monolayer $MoS_2$. (c) 1D potential energy in back-gate devices A, B, and C plotted with and without taking into effect IFBL.

back-gate oxide with a 1 nm EOT indicates a physically thicker $HfO_2$ than $SiO_2$. Thus at a given EOT, a high-$\kappa$ back-gate oxide leads to a larger depletion width due to increased screening of the fringing electric field, as also seen in the contour plot profiles. This result is further supported by the 1D cuts extracted from the 2D potential profiles in Fig. 3(g), which shows that at a given back-gate bias, the potential energy exhibits a sharp decline when the back-gate oxide is $SiO_2$ such as in A, consequently resulting in the thinnest depletion width [see the dotted oval in Fig. 3(g)]. It is followed by B which too has a low-$\kappa$ back-gate oxide but a high-$\kappa$ thick top oxide. The longest depletion width appears in C where both top and back-gate oxides are $HfO_2$. The smaller the depletion width the lower is the tunneling distance which increases the transmission probability and reduces the contact resistance as seen in geometry A.

The interplay between depletion width and contact resistance is observed in all the configurations across the chosen gate bias range. We show this in Fig. 4, where the red curve illustrates the contact resistance-ratios of configurations B and C to A in the absence of barrier lowering. Notably, as gate bias increases, the contact resistance shows an improvement. We find a considerable 75-fold and 20-fold rise in contact resistance for configurations C and B compared to configuration A when the effect of barrier lowering is excluded. This observation finds its origins in the reduction of the depletion width when surrounding dielectric environment is mostly low-$\kappa$.

We visualize the effect of IFBL on the contact resistance in A, B, and C by closely examining the blue curves in Fig. 4. The blue curve in Fig. 4 denotes the ratio of the contact resistances of A, B, and C with and without IFBL. We find that A shows the strongest effect of barrier lowering with 8 times improvement in contact resistance whereas there is only about three and five times improvement in C and B, respectively. Similarly in Fig. 3(g), we see that a gate bias of 1 V, the barrier lowering is worst in C and best in A. Moreover, the proximity of the metal-gate helps in lowering the barrier height. So, at a given EOT low-$\kappa$ insulators lower the height of the barrier more than high-$\kappa$ oxides and nearby gates help.

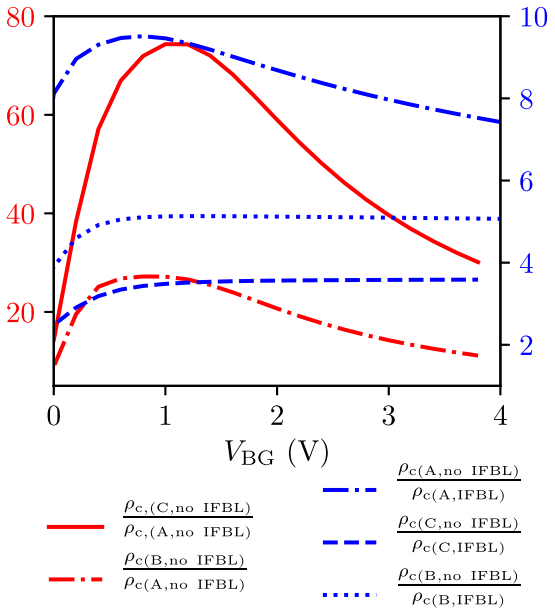


FIG. 4. Ratio of contact resistances in configurations A, B, and C with and without IFBL, as a function of back-gate bias.

Figure 5 shows the inverse image potential energy with respect to $x$, which can be thought of as a "position-dependent dielectric constant," where $x$ is the distance of the point charge from the metal-TMD interface, and $V_{\text{image}}(x)$ is the calculated image potential for a point charge located in the middle of $MoS_2$ monolayer in the presence of different surrounding dielectrics. We see that at distances much larger than the layer thickness ($x \gg t_{2D}$), the inverse of the image potential is determined by the back gate. This is in contrast to the case without back gate, where the inverse potential is determined by the dielectric constant of the surrounding oxide. However, when $x \ll t_{2D}$, the 2D-material dielectric constant dominates, as in the bulk case, and the barrier-lowered potential behaves as $\epsilon_{2D}x$. This figure thereby implies that the barrier lowering is screened by the back gate which deters the improvement in contact resistance in electrostatically doped edge contacts.

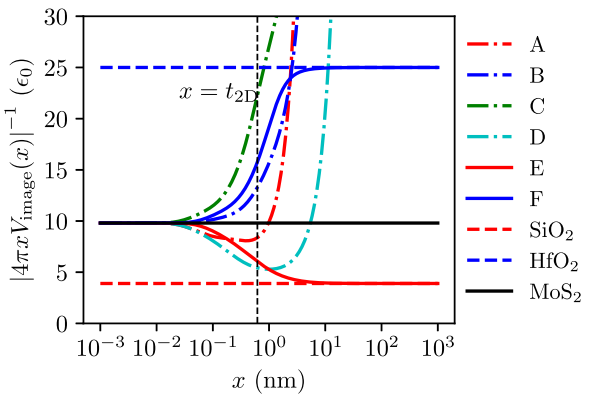


FIG. 5. Inverse of image potential energy plotted as a function of the distance from the metal-TMD interface. Low values of $[4\pi x V_{\text{image}}(x)]^{-1}$ means improved IFBL and therefore E and A have the best cases of barrier lowering.

## IV. CONCLUSION

We have numerically evaluated the contact resistance of back-gated metal-TMD edge contacts. We have investigated the effect of both low-$\kappa$ and high-$\kappa$ bottom oxides with similar EOT. Our results indicate that low-$\kappa$ back-gate oxides result in a lower contact resistance, although the concern of gate leakage remains. Applying a sufficiently high gate bias (>1V) can result in favorable contact resistance (50 Ω μm) when using a high–$\kappa$ dielectric such as $HfO_2$ as the back-gate oxide. In our simulations, we have accounted for the semiconductor doping through back-gate bias. Upon comparing our results with the contact resistances in impurity-doped edge-contacts we observed that electrostatically doped edge contacts do not provide significant benefits.

It should be noted that we simulated the band structure of an isolated monolayer of $MoS_2$ to calculate the transmission. A more accurate electronic structure of the interfaces requires DFT simulations of the entire $MoS_2$-oxide-metal structure which is beyond the scope of this paper. It is important to note that the type of oxides, and oxide-$MoS_2$ terminations, simply determines the Fermi level position of the semiconductor, affecting its n or p-type characteristics, similar to the effect of doping a semiconductor [51,52]. The edge-contact termination at the metal-$MoS_2$ interface determines the charge transfer between the metal and the semiconductor as well as the FLP [19]. The influence of surrounding oxides and doping via back-gate bias, on the contact resistance, predominantly stems from electrostatics, independent of the specific atomic arrangements at the $MoS_2$-oxide or metal interface. Indeed, our prior work utilizing effective-mass-based nonequilibrium Greens function (NEGF) simulations, has demonstrated that the impact of surrounding oxides on contact resistance outweighs that of metal-2D layer coupling [21].

We obtained our results assuming a 0.3 eV Schottky barrier without Fermi-level pinning (FLP). If large FLP is present, then this should be accounted for by changing the boundary conditions at the TMD in the Poisson equation compared to the rest of the metal. Considering two metals with the same work-function, the one with larger FLP would have a larger Schottky barrier height. However, considering two metals with the same effective Schottky barrier height, the metal with lower work-function will have higher FLP. In general, FLP should increase the electric field near the metal-$MoS_2$ junction and amplify the effect of the IFBL so that the same qualitative trends would be observed, albeit more pronounced. Since we compare different dielectric configurations for the same Schottky barrier, our investigation is fair and the findings will still hold qualitatively in the presence of FLP.

## ACKNOWLEDGMENTS

This work has been supported by the Taiwan Semiconductor Manufacturing Company, Ltd. and the NEWLIM-ITS/nCORE program of the Semiconductor Research Corporation (SRC). We also acknowledge the Texas Advanced Computing Center (TACC) at The University of Texas at Austin for providing the high-performance computing resources that have contributed to the research results reported within this paper [53].

[1] B. Radisavljevic, A. Radenovic, J. Brivio, I. V. Giacometti, and A. Kis, Single-layer $MoS_2$ transistors, Nat. Nanotechnol. **6**, 147 (2011).

[2] Q. H. Wang, K. Kalantar-Zadeh, A. Kis, J. N. Coleman, and M. S. Strano, Electronics and optoelectronics of two-dimensional transition metal dichalcogenides, Nat. Nanotechnol. **7**, 699 (2012).

[3] P. Miró, M. Audiffred, and T. Heine, An atlas of two-dimensional materials, Chem. Soc. Rev. **43**, 6537 (2014).

[4] L. Tao, E. Cinquanta, D. Chiappe, C. Grazianetti, M. Fanciulli, M. Dubey, A. Molle, and D. Akinwande, Silicene field-effect transistors operating at room temperature, Nat. Nanotechnol. **10**, 227 (2015).

[5] H. Liu, A. T. Neal, Z. Zhu, Z. Luo, X. Xu, D. Tománek, and P. D. Ye, Phosphorene: An unexplored 2D semiconductor with a high hole mobility, ACS Nano **8**, 4033 (2014).

[6] V. Podzorov, M. Gershenson, C. Kloc, R. Zeis, and E. Bucher, High-mobility field-effect transistors based on transition metal dichalcogenides, Appl. Phys. Lett. **84**, 3301 (2004).

[7] S. Das, H.-Y. Chen, A. V. Penumatcha, and J. Appenzeller, High performance multilayer $MoS_2$ transistors with scandium contacts, Nano Lett. **13**, 100 (2013).

[8] D. Jariwala, V. K. Sangwan, L. J. Lauhon, T. J. Marks, and M. C. Hersam, Emerging device applications for semiconducting two-dimensional transition metal dichalcogenides, ACS Nano **8**, 1102 (2014).

[9] S. Jo, N. Ubrig, H. Berger, A. B. Kuzmenko, and A. F. Morpurgo, Mono-and bilayer $WS_2$ light-emitting transistors, Nano Lett. **14**, 2019 (2014).

[10] Y.-F. Lin, Y. Xu, S.-T. Wang, S.-L. Li, M. Yamamoto, A. Aparecido-Ferreira, W. Li, H. Sun, S. Nakaharai, W.-B. Jian *et al.*, Ambipolar $MoTe_2$ transistors and their applications in logic circuits, Adv. Mater. **26**, 3263 (2014).

[11] F. Xia, H. Wang, and Y. Jia, Rediscovering black phosphorus as an anisotropic layered material for optoelectronics and electronics, Nat. Commun. **5**, 4458 (2014).

[12] S. Das and J. Appenzeller, Where does the current flow in two-dimensional layered systems? Nano Lett. **13**, 3396 (2013).

[13] H. Liu, M. Si, Y. Deng, A. T. Neal, Y. Du, S. Najmaei, P. M. Ajayan, J. Lou, and P. D. Ye, Switching mechanism in single-layer molybdenum disulfide transistors: An insight into current flow across Schottky barriers, ACS Nano **8**, 1031 (2014).

[14] Y. Guo, Y. Han, J. Li, A. Xiang, X. Wei, S. Gao, and Q. Chen, Study on the resistance distribution at the contact between molybdenum disulfide and metals, ACS Nano **8**, 7771 (2014).

[15] A. Allain, J. Kang, K. Banerjee, and A. Kis, Electrical contacts to two-dimensional semiconductors, Nat. Mater. **14**, 1195 (2015).

[16] D. S. Schulman, A. J. Arnold, and S. Das, Contact engineering for 2D materials and devices, Chem. Soc. Rev. **47**, 3037 (2018).

[17] D. Cakır and F. M. Peeters, Dependence of the electronic and transport properties of metal-$MoSe_2$ interfaces on contact structures, Phys. Rev. B **89**, 245403 (2014).

[18] L. Jelver, D. Stradi, K. Stokbro, and K. W. Jacobsen, Schottky barrier lowering due to interface states in 2D heterophase devices, Nanoscale Adv. **3**, 567 (2021).

[19] K. Parto, A. Pal, T. Chavan, K. Agashiwala, C.-H. Yeh, W. Cao, and K. Banerjee, One-Dimensional edge contacts to two-dimensional Transition-Metal dichalcogenides: Uncovering the role of schottky-Barrier anisotropy in charge transport across $MoS_2$/Metal Interfaces, Phys. Rev. Appl. **15**, 064068 (2021).

[20] Á. Szabó, A. Jain, M. Parzefall, L. Novotny, and M. Luisier, Electron transport through metal/$MoS_2$ interfaces: Edge- or area-dependent process? Nano Lett. **19**, 3641 (2019).

[21] M. Brahma, M. L. Van de Put, E. Chen, M. V. Fischetti, and W. G. Vandenberghe, The importance of the image forces and dielectric environment in modeling contacts to two-dimensional materials, npj 2D Mater. Appl. **7**, 14 (2023).

[22] E. Xu, H. Liu, K. Park, Z. Li, Y. Losovyj, M. Starr, M. Werbianskyj, H. Fertig, and S. Zhang, p-Type transition-metal doping of large-area $MoS_2$ thin films grown by chemical vapor deposition, Nanoscale **9**, 3576 (2017).

[23] S. Wang, H. Li, H. Sawada, C. S. Allen, A. I. Kirkland, J. C. Grossman, and J. H. Warner, Atomic structure and formation mechanism of sub-nanometer pores in 2D monolayer $MoS_2$, Nanoscale **9**, 6417 (2017).

[24] D. Rhodes, D. Chenet, B. Janicek, C. Nyby, Y. Lin, W. Jin, D. Edelberg, E. Mannebach, N. Finney, A. Antony *et al.*, Engineering the structural and electronic phases of $MoTe_2$ through W substitution, Nano Lett. **17**, 1616 (2017).

[25] E. Kim, C. Ko, K. Kim, Y. Chen, J. Suh, S.-G. Ryu, K. Wu, X. Meng, A. Suslu, S. Tongay *et al.*, Site selective doping of ultrathin metal dichalcogenides by laser-assisted reaction, Adv. Mater. **28**, 341 (2016).

[26] L. Yang, K. Majumdar, H. Liu, Y. Du, H. Wu, M. Hatzistergos, P. Hung, R. Tieckelmann, W. Tsai, C. Hobbs *et al.*, Chloride molecular doping technique on 2D materials: $WS_2$ and $MoS_2$, Nano Lett. **14**, 6275 (2014).

[27] J. Gao, Y. D. Kim, L. Liang, J. C. Idrobo, P. Chow, J. Tan, B. Li, L. Li, B. G. Sumpter, T.-M. Lu *et al.*, Transition-metal substitution doping in synthetic atomically thin semiconductors, Adv. Mater. **28**, 9735 (2016).

[28] K. Zhang, B. M. Bersch, J. Joshi, R. Addou, C. R. Cormier, C. Zhang, K. Xu, N. C. Briggs, K. Wang, S. Subramanian *et al.*, Tuning the electronic and photonic properties of monolayer $MoS_2$ via *in situ* rhenium substitutional doping, Adv. Funct. Mater. **28**, 1706950 (2018).

[29] H. Li, X. Duan, X. Wu, X. Zhuang, H. Zhou, Q. Zhang, X. Zhu, W. Hu, P. Ren, P. Guo *et al.*, Growth of alloy $MoS_{2x}Se_{2(1-x)}$ nanosheets with fully tunable chemical compositions and optical properties, J. Am. Chem. Soc. **136**, 3756 (2014).

[30] C. Huang, S. Wu, A. M. Sanchez, J. J. Peters, R. Beanland, J. S. Ross, P. Rivera, W. Yao, D. H. Cobden, and X. Xu, Lateral heterojunctions within monolayer $MoSe_2$–$WSe_2$ semiconductors, Nat. Mater. **13**, 1096 (2014).

[31] V. P. Pham and G. Y. Yeom, Recent advances in doping of molybdenum disulfide: Industrial applications and future prospects, Adv. Mater. **28**, 9024 (2016).

[32] Y. Li, C.-Y. Xu, P. Hu, and L. Zhen, Carrier control of $MoS_2$ nanoflakes by functional self-assembled monolayers, ACS Nano **7**, 7795 (2013).

[33] M. Yamamoto, S. Nakaharai, K. Ueno, and K. Tsukagoshi, Self-limiting oxides on $WSe_2$ as controlled surface acceptors and low-resistance hole contacts, Nano Lett. **16**, 2720 (2016).

[34] D. Qu, X. Liu, M. Huang, C. Lee, F. Ahmed, H. Kim, R. S. Ruoff, J. Hone, and W. J. Yoo, Carrier-type modulation and mobility improvement of thin $MoTe_2$, Adv. Mater. **29**, 1606433 (2017).

[35] M. A. Khan, M. F. Khan, S. Rehman, H. Patil, G. Dastgeer, B. M. Ko, and J. Eom, The non-volatile electrostatic doping effect in $MoTe_2$ field-effect transistors controlled by hexagonal boron nitride and a metal gate, Sci. Rep. **12**, 12085 (2022).

[36] F. Wang, Z. Wang, C. Jiang, L. Yin, R. Cheng, X. Zhan, K. Xu, F. Wang, Y. Zhang, and J. He, Progress on electronic and optoelectronic devices of 2D layered semiconducting materials, Small **13**, 1604298 (2017).

[37] J. Wang, X. Zou, X. Xiao, L. Xu, C. Wang, C. Jiang, J. C. Ho, T. Wang, J. Li, and L. Liao, Floating gate memory-based monolayer $MoS_2$ transistor with metal nanocrystals embedded in the gate dielectrics, Small **11**, 208 (2015).

[38] S. Ravandi, B. Fu, W. G. Vandenberghe, S. J. Aboud, and M. V. Fischetti, in *Proceedings of the 16th International Workshop on Computational Electronics* (Society for Micro- and Nanoelectronics, Nara, Japan, 2013).

[39] A. A. Mostofi, J. R. Yates, G. Pizzi, Y.-S. Lee, I. Souza, D. Vanderbilt, and N. Marzari, An updated version of wannier90: A tool for obtaining maximally localized Wannier functions, Comput. Phys. Commun. **185**, 2309 (2014).

[40] M. S. Alnæs, J. Blechta, J. Hake, A. Johansson, B. Kehlet, A. Logg, C. Richardson, J. Ring, M. E. Rognes, and G. N. Wells, The FEniCS Project Version 1.5, Arch. Numer. Softw. **3**, 9 (2015).

[41] A. Logg, K. A. Mardal, and G. N. Wells, *Automated Solution of Differential Equations by the Finite Element Method: The FEniCS Book* (Springer, Berlin, 2012).

[42] A. Laturia, M. L. Van de Put, and W. G. Vandenberghe, Dielectric properties of hexagonal boron nitride and transition metal dichalcogenides: From monolayer to bulk, NPJ 2D Mater. Appl. **2**, 6 (2018).

[43] G. Kresse and J. Hafner, *Ab initio* molecular dynamics for liquid metals, Phys. Rev. B **47**, 558 (1993).

[44] G. Kresse and J. Hafner, *Ab initio* molecular-dynamics simulation of the liquid-metal–amorphous-semiconductor transition in germanium, Phys. Rev. B **49**, 14251 (1994).

[45] G. Kresse and J. Furthmüller, Efficient iterative schemes for *ab initio* total-energy calculations using a plane-wave basis set, Phys. Rev. B **54**, 11169 (1996).

[46] G. Kresse and J. Furthmüller, Efficiency of *ab initio* total energy calculations for metals and semiconductors using a plane-wave basis set, Comput. Mater. Sci. **6**, 15 (1996).

[47] G. Kresse and D. Joubert, From ultrasoft pseudopotentials to the projector augmented-wave method, Phys. Rev. B **59**, 1758 (1999).

[48] J. P. Perdew, K. Burke, and M. Ernzerhof, Generalized gradient approximation made simple, Phys. Rev. Lett. **77**, 3865 (1996).

[49] S. Grimme, J. Antony, S. Ehrlich, and H. Krieg, A consistent and accurate *ab initio* parametrization of density functional dispersion correction (DFT-D) for the 94 elements H-Pu, J. Chem. Phys. **132**, 154104 (2010).

[50] J. Heyd, G. E. Scuseria, and M. Ernzerhof, Hybrid functionals based on a screened Coulomb potential, J. Chem. Phys. **118**, 8207 (2003).

[51] A. Valsaraj, J. Chang, A. Rai, L. F. Register, and S. K. Banerjee, Theoretical and experimental investigation of vacancy-based doping of monolayer $MoS_2$ on oxide, 2D Mater. **2**, 045009 (2015).

[52] K. Dolui, I. Rungger, and S. Sanvito, Origin of the n-type and p-type conductivity of $MoS_2$ monolayers on a $SiO_2$ substrate, Phys. Rev. B **87**, 165402 (2013).

[53] http://www.tacc.utexas.edu